Nanoscale

Accepted Manuscript

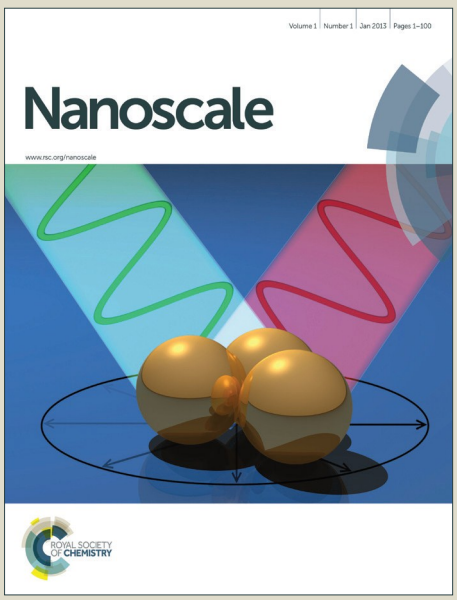

ROYAL SOCIETY OF CHEMISTRY

www.rsc.org/nanoscale

Phonon Transport at the Interfaces of Vertically Stacked Graphene and Hexagonal Boron Nitride Heterostructures

Zhequan Yan[1], Liang Chen[2], Mina Yoon[3] and Satish Kumar[1]

[1]*G.W. Woodruff School of Mechanical Engineering, Georgia Institute of Technology, Atlanta, GA, United States*

[2]*School of Energy and Power Engineering, Xi'an Jiaotong University, Xi'an, Shaanxi, PR China*

[3]*Center for Nanophase Materials Sciences, Oak Ridge National Laboratory, Oak Ridge, TN, USA*

Hexagonal boron nitride (h-BN) is a promising substrate for the graphene based nano-electronic devices. We investigate ballistic phonon transport at the interface of vertically stacked graphene and h-BN heterostructures using first principle density functional theory and atomistic Green's function simulations considering the influence of lattice stacking. We compute frequency and wave-vector dependent transmission function and observe distinct stacking-dependent phonon transmission features for the h-BN/graphene/h-BN sandwiched systems. We find that the in-plane acoustic modes have the dominant contributions to the phonon transmission and thermal boundary conductance (TBC) for the interfaces with the carbon atom located directly on top of the boron atom (C-B matched) because of the low interfacial spacing. The low interfacial spacing is a consequence of the differences in the effective atomic volume of N and B and the difference in the local electron density around the N and B. For the structures with the carbon atom directly on top of the nitrogen atom (C-N matched), the spatial distance increases and the contribution of in-plane modes to the TBC decreases leading to higher contributions by out-of-plane acoustic modes. We find that the C-B matched interfaces have stronger phonon-phonon coupling than the C-N matched interfaces, which results in the significantly higher TBC (more than 50%) in the C-B matched interface. The findings in this study will provide insights to

understand the mechanism of phonon transport at h-BN/graphene/h-BN interfaces, to better explain the experimental observations and to engineer these interfaces to enhance heat dissipation in graphene based electronic devices.

I. INTRODUCTION

Graphene as one of the remarkable two-dimensional (2D) materials exhibits exceptional thermal and electrical properties, which make it promising for many electronic applications such as high-frequency analog and RF devices [1-4]. Hexagonal boron nitride (h-BN) is an excellent dielectric substrate for graphene devices owing to its planar hexagonal lattice structure and atomically smooth surface. H-BN has a small lattice mismatch (less than 2%) with the graphene [5]. Graphene sandwiched between h-BN layers could remove the equivalence of two carbon atoms in a unit cell to open a band gap and change its electronic properties [6, 7]. For example, an order of magnitude higher electron mobility has been observed in the graphene/h-BN devices than in graphene/SiO_2 devices [5]. Therefore, h-BN has a potential to lead to breakthrough in the applications of graphene based devices.

As the device dimension scales down and power dissipation increases in electronic devices, inefficient thermal management can become challenging for performance and reliability [8]. Phonons are expected to be the dominant energy carriers for the interfacial thermal transport [9]. The acoustic phonons significantly contribute to heat transfer if the interfacial spacing is smaller than the phonon wavelength [10-12]. A fundamental understanding of phonon transport and thermal transport mechanism across graphene/h-BN interfaces is of great importance for improving heat dissipation and energy efficiency. Graphene/h-BN contact may play an important role in heat dissipation in its electronic devices [8]. But very low thermal boundary conductance (TBC) has

been reported using Raman spectroscopy technique, e.g., 7.4 MW/m^2·K for the single layer graphene/h-BN interface, which may become a critical challenge for high frequency applications of graphene such as FETs and interconnects [13]. However, only few studies have been focused on the prediction and analysis of TBC at graphene/h-BN interface. The TBC at multi-layer graphene (MLG)/h-BN interfaces has been calculated by Mao et al. [14] using the first principle method. The numerical simulations predict TBC as 186 MW/m^2·K, which is 24 times higher than the experimental value. One reason for this difference could be the roughness and contaminants at the interface or the defects of the samples which may influence the experimental results [15, 16]. Another reason could be that multi-layer graphene in numerical studies has different thermal properties compared with the single layer graphene (SLG) used in experiments [17, 18]. Furthermore, previous studies found that the lattice stacking patterns of graphene on bulk h-BN are different in different parts within the same flake of the samples, which is not the same as the assumption of "perfect" matching in the theoretical calculations [5, 19-21]. Therefore, the actual value of TBC across the graphene/h-BN interfaces is the comprehensive result of different lattice stacking configurations. Theoretically, there are twelve different possible lattice stacking configurations for graphene sandwiched by h-BN which could influence the electronic structures of SLG and lead to significant differences in bandgap [22-26]. Electron-phonon coupling in three typical stacking configurations is analyzed by Slotman et al. [27]. They found that the phonon modes dominated by the nitrogen atoms have the highest electron-phonon coupling constant which might be explained by the stronger force interactions between nitrogen and carbon than those between boron and carbon. However, the effects of lattice stacking on the phonon transmission, TBC and contribution of different phonon modes to TBC at the graphene/h-BN interfaces are not well understood yet.

In this work, we investigate the ballistic phonon transport at the interface of SLG sandwiched by h-BN layers in different lattice stacking configurations. First principle density functional theory (DFT) and atomistic Green's function (AGF) simulations are used to investigate the phonon transmission and TBC of h-BN/SLG/h-BN interfaces. Five representative configurations are chosen from the twelve possible lattice stacking configurations. We analyze the phonon dispersion relations and density of states (DOSs) of SLG sandwiched by the h-BN layers in different lattice stacking configurations. The h-BN substrates soften the TO and LO modes of graphene and open a significant gap between the TA and ZA modes at K point. We, for the first time, report both frequency and wave-vector (k space) dependent transmission for graphene/h-BN interfaces and analyze the contribution of different phonon modes to TBC in different configurations. We find that the low frequency in-plane acoustic modes have the dominant contributions to the TBC in the configurations with low interfacial spacing between graphene and h-BN. For the configurations with higher interfacial gap, the relative contribution of in-plane modes to TBC decreases and contribution of out-of-plane acoustic modes increases. Furthermore, the interfaces with the carbon atom directly on top of the boron atom (C-B matched) have better phonon-phonon coupling between graphene and h-BN than those with the carbon atom directly on top of the nitrogen atom (C-N matched). The TBC can be enhanced by more than 50% by changing the lattice stacking arrangements from C-N match to C-B match. Our results for TBC (32.5~50.0 $MW/m^2 \cdot K$) is closer to the experimental measurement (3.7 = 0.5×7.4 $MW/m^2 \cdot K$ [13] projected for two sided interface in sandwiched structure) compared to the previous studies [14].

Ⅱ. MODELS AND COMPUTATIONAL METHODS

In this study, we restrict our investigation to only five typical lattice stacking h-BN/SLG/h-BN sandwiched structures. They are representative lattice stacking arrangements for their symmetry and combinations [22, 25]. We optimize these sandwiched structures by DFT calculations [28]. The phonon transmission functions across the h-BN/graphene/h-BN interfaces are calculated by AGF calculation, and the TBCs are obtained using the Landauer formula [17, 29-31]. In AGF calculations, the second order interatomic force constants (IFCs) are directly obtained from DFT calculations for a reliable prediction of the atomic interactions at interfaces [31, 32]. In this study, we limit the temperature to 300K, which is much lower than the Debye temperature of the graphene (~2100K [33]) and h-BN (~1740K [34]). It has been shown before that including the third order force constants at the interface doesn't show large effect on the interfacial thermal conductance [35]. Considering high complexity in incorporating anharmonic effects (three phonon scattering) in the AGF formulation and its relatively low contributions to TBC at low temperatures, we have not considered these affects in our simulation. Similar approach, with harmonic phonon transport assumption, has been used in many previous studies [36-40]. Details of AGF calculation will be discussed in Section B. Figure 1 shows two side views, in x-y plane and x-z plane, of different lattice stacking configurations of SLG sandwiched between h-BN layers. We distinguish them as ABA(B), ABA(N), ABC(B), ABC(N,B), AAA. The two bulk h-BNs in structure ABA(B) and ABA(N) are mirror symmetry about the graphene layer. For structure ABA(B), the B in the parentheses presents that the boron atom is on the top of one carbon atom in the unit cell, while the nitrogen atom is centered above the graphene ring. The difference between ABC(B) and ABA(B) is that the boron atoms on both sides of the graphene in ABC(B) is on top of different carbon atoms in the unit cell. The structure ABC(N,B) is a combination of

ABA(N) and ABA(B). To the left side of the graphene, it has the same stacking configuration with ABA(N), while the right side is same with ABA(B). In structure AAA, h-BN is completely aligned with graphene with one boron atom over one carbon atom and one nitrogen atom over another carbon atom in the unit cell. Figure 2 shows the schematic of a typical h-BN/SLG/h-BN structure considered in the AGF calculations.

A. Density functional theory calculations

We use the Vienna ab initio simulation package (VASP) to perform the DFT calculations [28, 41]. A plane wave basis set and the projector augmented-wave (PAW) method are used with the local density approximation (LDA) exchange–correlation functional [42, 43]. The LDA shows a reasonable structural properties for the system near the equilibrium [41, 44], especially for the interlayer distance in systems like graphite [45] and h-BN [46], although LDA tends to underestimate the interlayer binding energies and band gaps of graphite and h-BN due to the lack of description of van der Waals forces, which are the manifestation of long-range correlation effects [21, 22, 47]. Interfacial TBC in this study is a highly interlayer distance dependent property, and LDA reveals a very good performance in calculating interlayer distance and force constants [14, 17, 21]. The optimized in-plane lattice constant of graphene and bulk h-BN are $a_{\mathrm{SLG}} = 2.45\,\text{Å}$, $a_{\text{h-BN}} = 2.49\,\text{Å}$ and $c_{\text{h-BN}} = 3.26\,\text{Å}$ which are in good agreement with the simulation and experimental results from the previous studies [21, 48, 49]. We use the lattice constant of h-BN ($a = 2.49$ Å) in the sandwiched systems, where the SLG is under less than 2% strain. We set a kinetic energy cutoff of 500 eV and a 25×25×1 k-point grid to optimize the h-BN/graphene/h-BN sandwiched structures. The unit cell of these sandwiched structures contains two carbon atoms, eight h-BN layers with one boron and one nitrogen atoms in each layer [Fig. 1]. The distance between the graphene and h-BN substrates is optimized for the unit cell system shown in Fig. 1. Using this

optimized equilibrium structure, a 5x5 supercell of a graphene sheet sandwiched by 8 layers of h-BN bulks [Fig. 2] is assembled for the calculations of the second order IFCs. This supercell contains 450 atoms and a vacuum region of 16 Å. We apply 3×3×1 k-point grids to sample the Brillouin zone of this supercell. For IFCs of the h-BN bulk, we use a 5×5×4 supercell with the periodic boundary conditions and 3×3×1 k-point grids. To calculate the IFCs, we displace each atom in a unit cell into two directions: one in plane and one orthogonal to the plane of the graphene layer. The displacement length is 0.01 Å. The kinetic energy cutoff of the 5×5 supercell is 450 eV. The system energy convergence criterion is set to be 1e-6 eV. The force convergence criterion is set to be -0.01eV/Å. Then, with the IFCs obtained from the DFT calculations, we construct the harmonic matrices which describe the interatomic interactions in the AGF calculations.

B. Atomistic Green's function calculations

We obtained the transmission function and TBC from AGF calculations [17, 50], where graphene ('device') is sandwiched between two 'contacts' corresponding to the hot and cold thermal reservoirs represented by semi-infinite h-BN bulks [Fig. 2]. The heat flux J through the system carried by phonons is evaluated by Landauer formalism [30, 51]

$$J = \int_0^\infty \int_{\vec{k}_\parallel} \frac{\hbar\omega}{2\pi}\left[N_L\left(\omega,T\right) - N_R\left(\omega,T\right)\right] \Xi\left(\omega,\vec{k}_\parallel\right) \frac{d\vec{k}_\parallel}{\left(2\pi\right)^2} d\omega \qquad (1)$$

where $N\left(\omega,T\right)$ is the Bose-Einstein distribution function at frequency ω and temperature T. The subscript L and R mean the left and right contact. If the temperature difference between the contacts is sufficiently small, the phonon occupation difference in Eq. (1) becomes

$$N_L(\omega,T)-N_R(\omega,T)=\frac{\hbar\omega}{k_BT^2}\frac{e^{\hbar\omega/k_BT}}{\left(e^{\hbar\omega/k_BT}-1\right)^2}\Delta T \quad (2)$$

$\Xi\left(\omega,\vec{k}_{\parallel}\right)$ is the transmission function at frequency ω and transverse k-point $\vec{k}_{\parallel}$.

$$\Xi\left(\omega,\vec{k}_{\parallel}\right)=\mathrm{Trace}\left[\Gamma_L G_{LD,RD}\Gamma_R G_{LD,RD}^{T}\right] \quad (3)$$

Where $G_{LD,RD}$ and $G_{LD,RD}^{T}$ are the part of the Green's function of device region and its complex conjugate. Γ_L and Γ_R are the interfacial phonon escape rate from the left and right contacts. They are defined as

$$\Gamma_{L(R)}\left(\omega,\vec{k}_{\parallel}\right)=i\left(\tau_{L(R)}-\tau_{L(R)}^{T}\right) \quad (4)$$

$\tau_{L(R)}$ shows the change of phonon dynamical behavior caused by the left (right) contact, which is the element of the Self-energy matrix in the sandwiched system's Green's function [30]. We construct the harmonic matrices in a finite plane-wave form so that an efficient sampling in transverse Brillouin zone $\vec{k}_{\parallel}$ can be used to include the phonons of all wavelengths [29]. The Monkhorst-Pack scheme [52] is used to discretize the Brillouin zone with the mesh of 401×401. We compute frequency and wave vector (k space) dependent transmission $\Xi\left(\omega,\vec{k}_{\parallel}\right)$ which shows angular symmetry in the Brillouin zone. So, we present $\Xi\left(\omega,\vec{k}_{\Gamma-K}\right)$ along $\Gamma-K$ direction which is also convenient to compare with the phonon dispersion along $\Gamma-K$ in a same figure. These results give us a detailed understanding of phonon mode contributions to the TBC. Finally, we can obtain the TBC (σ) using the definition

$$\sigma=\frac{J}{\Delta T} \quad (5).$$

Ⅲ. RESULTS AND DISCUSSIONS

After the structural optimization, the interfacial separation distance is 3.23Å for the ABA(B) and ABC(B), 3.45Å for the ABA(N), 3.51Å for the AAA. The ABC(N,B) has the interfacial separation distance of 3.45Å at one side and 3.23Å at the other side because of the different configurations on different sides of the graphene layer. The structural optimization has a good agreement with the results from the previous studies [20-22, 53]. For example, Giovannetti's group [21] used the LDA as the exchange–correlation functional to calculate the interfacial separation distance of graphene/h-BN. For the structure ABA(B), ABA(N) and AAA, the value is 3.22Å, 3.40Å and 3.50 Å, respectively. Some important results of h-BN/graphene/h-BN sandwiched structure with different lattice stacking arrangements are shown in Table 1.

A. Phonon dispersion relations and Density of states (DOS)

Figure 3 shows the phonon dispersion of SLG, which is determined by diagonalizing the dynamical matrix of IFCs from the DFT calculations. Figure 3(a-e) compare the phonon dispersions of stretched and isolated SLG with the stretched SLG in the system of h-BN/SLG/h-BN with different stacking configurations. To decipher the different mechanisms that influence the phonon dispersion we added the phonon dispersion relation of isolated SLG, un-stretched with equilibrium lattice constant (2.45Å), in Fig. 3(a) for comparison. In Fig. 3(a), the phonon dispersion relations show that stretching the isolated SLG will strongly soften the LO (Longitudinal optical) and TO (Transverse optical) modes for the entire $\Gamma-K$ branch. In addition, there is a softening in LA (Longitudinal acoustic) mode compared with the un-stretched and isolated SLG. That is because stretching the SLG will increase the C-C bond length which will weaken the C-C bond and decrease the in-plane stretching force constant [54]. However, when we introduced the h-BN substrates, where SLG lattice is stretched to the h-BN lattice, the

phonon dispersions reveal a further softening in LO and TO mode especially at the Γ point compared to the stretched isolated SLG. The additional "weakening" of the phonon vibrational modes LO and TO is initiated by the hybridization of graphene's out-of-plane π bond and h-BN's π bond. In graphene, the out-of-plane $2p_z$ orbitals are half-filled and the π band is half full, while in the h-BN, the $2p_z$ orbitals are either empty or full. The mixing of h-BN's $2p_z$ orbitals with those of graphene will change the occupation in the graphene's π states which results in further weakening of the C-C bond. A similar effect was observed in graphene on metal substrates, because the charge transfer happened from metal's *d* orbital to graphene's π states [54-56].

In Fig. 3(a-e), a splitting between ZA and ZO modes can be observed at K point in most structures except ABC(B). The splitting is caused by breaking the equivalent of graphene's two carbon atoms in a unit cell [57]. For example, the structure ABA(B) introduces two bulks of h-BN on both sides of the graphene, with one carbon atom on top of the boron atom and the other carbon atom on the hollow of the h-BN ring. In other words, the carbon directly on top of the h-BN atoms will have a stronger interaction with h-BN than the other carbon atom. The AAA structure with the stacking of two carbon atoms on either boron or nitrogen atoms has the largest ZA/ZO splitting at K point, because the repulsion and attraction from both sides of the interface by either nitrogen or boron atoms enhance the asymmetry of the two carbon atoms. However, the ABC(B) structure shows no ZA/ZO splitting at K point because of the centrosymmetric matching configuration on both sides of the graphene. The ZA/ZO splitting values for different configurations are shown in Table 1. Furthermore, Fig. 3(a-e) shows a shift of the ZA mode at Γ point when graphene is sandwiched by h-BN. The shift of ZA mode at Γ point indicates the strength of the spring constant at the interfaces [48, 57].

In order to investigate the effects of lattice stacking of h-BN/SLG/h-BN on phonon distribution, we calculate the phonon DOS of the SLG sandwiched by h-BN in different stacking configurations. Figure 4 compares the DOSs of isolated SLG, stretched isolated SLG, h-BN and SLG (stretched) sandwiched by h-BN in different stacking configurations. The results show that stretching the isolated SLG lower the cut-off frequency of DOSs. The sandwiched structure develops a new peak around 46 THz [highlighted by an arrow in Fig. 4]. It corresponds to the softening of the LO and TO modes at Γ point resulting from the interactions with the bulk h-BN substrates. The impact of lattice stacking on the DOSs of SLG is negligible as different stacking configurations results in almost identical DOS. Compared with the un-stretched isolated SLG, the DOSs of sandwiched SLG is suppressed near zero frequency (< 2 THz) and then increases rapidly with a small overshoot near 3THz which is signature of shift of ZA mode near the Γ point. In addition, phonon spectrum mismatch between graphene and h-BN at high frequencies can be observed by comparing their DOSs (Fig.7). We find that the DOS mismatch between graphene and h-BN results in a small phonon transmission in the high frequency region (> 10 THz). More details will be discussed in Section C.

B. Thermal boundary conductance

Following the Landauer formalism (Eq. 1), we obtained the temperature dependent and frequency dependent TBC of the five lattice stacking h-BN/SLG/h-BN configurations [Fig. 5(a, b)]. The results show that the TBC at room temperature is in the range of 32.5~50.0 MW/m^2·K depends on the stacking configurations in the order of ABC(B)>ABA(B)>AAA> ABC(N,B)>ABA(N) (Table 1). With the exception of the structure AAA (43.1 MW/m^2·K)[More details will be explained in section C.], the order of the TBC's magnitude is consistent with the inverse order of interfacial separation distance:

ABC(B)<ABA(B)<ABC(N,B)<ABA(N). The stacking configurations with C-B matched interfaces (boron atom on top of the carbon atom, such as in the ABC(B), and ABA(B)) have larger TBCs (50.0 and 46.6 MW/m^2·K) because of the smaller interfacial separation distances. The stacking configurations with C-B matched interfaces (ABC(B), ABA(B)) also have the lowest binding energy and the best structural stability. However, ABC(B) exhibits a virtually negligible electronic band gap in graphene because the centrosymmetric stacking is unable to break the equivalence of the two carbon atoms [22, 58]. Therefore, ABA(B)-stacked structure with TBC very close to ABC(B) can be considered to be the best configuration for the nano-electronic devices from the perspective of achieving good thermal and electric properties. Controlling the interfacial geometry can enhance the TBC and heat dissipation in nano-electronic devices.

To understand the origin of the dependence of the TBC to the interfacial separation distance, we calculate the plane-averaged electron density difference Δn which will also help in visualizing the electron redistribution upon the lattice stacking of the interfaces [Fig. 6]. We define the plane-averaged electron density difference Δn as

$$\Delta n(z) = \Delta n_{\text{sandw}}(z) - \Delta n_{\text{BN}}(z) - \Delta n_{\text{SLG}}(z) \quad (6)$$

where $\Delta n_{\text{sandw}}(z)$, $\Delta n_{\text{BN}}(z)$, $\Delta n_{\text{SLG}}(z)$ indicate the plane-averaged densities of the sandwiched structure, h-BN layers and free-standing graphene, respectively. To keep consistent with the IFCs calculations, LDA is still used as the exchange-correlation functional. Although LDA tends to underestimate the interlayer binding energies and band gaps [21, 22], it is still a good approximation to predict structural parameters and the trend of electron density difference [41]. The details of the calculation can be found in Ref. [59]. Figure 6 shows that as interfacial separation distance decreases (from ABA(N) to ABA(B)), the magnitude of the plane-averaged electron density

difference increase rapidly. This indicates that the electron wave functions of both graphene and h-BN have a stronger overlap at the interfacial gap as the separation distance decreases. This overlap was also observed by Xiong et al.'s [10], which is in agreement with our analysis of dispersion relations in the previous section.

The ABC(N,B)-stacked configuration is a combination of ABA(B) and ABA(N) arrangement, and reveals an intermediate TBC (40.8 MW/m^2·K). However, the AAA-stacked structure shows a larger TBC (43.1 MW/m^2·K) despite its largest interfacial separation distance even compared to the ABA(N). The phonon transport mechanism at interfaces will be discussed in detail in the next section. Our results (TBC 32.5~50.0 MW/m^2·K) are closer to the experimental measurement (3.7 ~ 0.5×7.4 MW/m^2·K[13]) compared to other studies (93 ~ 0.5×186 MW/(m^2·K)[14]), but difference is still large. One reason could be the quality of the samples in experiment. The corrugation and defects on the graphene samples, and the roughness and the contaminants at the interface may significantly decrease the TBC. Another reason could be the limitations and uncertainty in the Raman spectroscopy measurement in estimating heat flux across the interface [60]. In addition, the graphene and h-BN are not perfectly matched in the experiments. Different orientations of the two lattice in same sample and lattice mismatch [19] could lower the TBC [61]. While our simulation is based on five different lattice stacking configurations. Each of them correspond to a perfect interface made by stretching the graphene to fit the h-BN's lattice constant. The developed models and related analysis seek to decipher the mechanism of the phonon transport at the interface which is the focus of our study.

C. Phonon transmission and contribution

To explain the anomaly in the order of TBC with the interfacial separation distance, such as structure AAA, and to understand the mechanism of phonon transport at interface, we calculate

the frequency dependent phonon transmission functions across h-BN/SLG/h-BN interfaces in all five configurations under consideration [Fig. 7]. Figure. 7 clearly shows that the interfacial transmission is dominated by low-frequency (< 5THz) phonons. We find that the DOS mismatch between graphene and h-BN results in a small phonon transmission in the high frequency region. The transmission peak in the high frequency region is located around 10THz, 20THz and 40THz, which is consistent with the positions of the peaks of phonon DOS in h-BN but the transmission is low as peaks in DOSs of graphene are not co-located and these high frequency phonons may not efficiently couple. Since the high frequency transmissions make little contribution to the TBC because of the low temperature, we focus more on the phonon transmission under 10THz, which make the dominant contribution to the TBC. In the low frequency region, we observe two transmission peaks and one valley for each structure. The valley between the two peaks is around 2.5 THz for structures ABA(B), AAA, ABC(B), ABC(N,B). However, for the structure ABA(N), there exists a broader valley around 2.5~3.1 THz, and the high frequency peak [the blue solid arrow in Fig. 7] is much narrower than the low frequency peak. In contrast, structure ABA(B) has a much wider high frequency peak, indicated by the black solid arrow. In order to explain this, we compute the phonon transmission function in the first Brillouin zone of the unit cell [Fig. 8]. In Fig. 8, we present the phonon transmission along the Γ-K direction in k space for different frequencies and analyze the relative transmission of phonon modes across the interfaces. The color changes from dark blue to red show the increase of the phonon transmission strength. Different phonon modes of graphene [Fig. 8(a-e)] and the whole system [Fig. 8(f-j)] are shown on top of the transmission contours. The graphene's phonon modes in Fig. 8(a-e) were calculated by solving the 6×6 dynamic matrix which is a part of the system's 54×54 dynamic matrix, and

belongs to the two carbon atoms in the system. Black dots in Fig. 8(f-j) show the phonon modes of the sandwiched structure by solving the entire dynamic matrix of the system.

For configurations with low interfacial separation distance [C-B matched interfaces, Fig. 8(a, d) and Table-1], the in-plane acoustic modes (the LA, TA modes) have the dominant contributions to the transmission. As the interfacial gap increases [Fig. 8(b)], the in-plane acoustic modes' contribution decreases leading to higher contributions by out-of-plane acoustic modes (~ZA modes). This could be further understood by the frequency dependent TBC from Fig. 5 (b) and wave-vector dependent transmission from Fig. 8. Compared to the ABA(B) configuration in Fig.5(b), the slope of the ABA(N)'s TBC ~ frequency curve decreases sharply after 2 THz. This is because of very low transmission between 2-3 THz for ABA(N) compared to ABA(B) as shown in Figs. 8 (a) and (b). In addition, TBC difference between AAA and ABA(B) increases after 2 THz [Fig. 5(b)] resulting from the weakening of the contribution to transmission from LA and TA modes shown in Fig. 8(c). However, the configuration AAA with a 3.50 Å interfacial gap have better transmission and larger TBC than the ABA(N) with a 3.45 Å interfacial gap. Despite of the higher interfacial separation distance, the TBC is higher because of the better phonon coupling between graphene and h-BN in structure AAA than that in the ABA(N). We found that the interfaces with C atoms directly on top of B atoms has stronger phonon-phonon coupling between graphene and h-BN than that with C atom directly on top of N atom. One explanation for this is that the mass of the B atom is much closer to the C atom than the N atom. The mass difference of B and C is 37.5% smaller than that of N and C, which leads to closer vibration frequency for energy transfer. An additional explanation for this observation is that the short-range Pauli's repulsive forces acting on the C-N matched layer is larger than that of C-B matched layer due to differences in the effective atomic volume of N and B and the

difference in the local electron density around the N and B, which increases the separation distance and obstruct the phonon transmission. Therefore, the C-B matching in the AAA configuration in addition to C-N matching leads to higher transmission and TBC compared to the C-N matched structure ABA(N). Furthermore, by considering the eigenvectors of the sandwiched system's dynamic matrix, we realize that the phonon modes with higher frequency involve more B atoms for the same wave vector, while the N atoms make more contributions to the lower frequency phonon modes. Similar observation for contribution of B and N atoms to phonon modes were made by Slotman et al.'s [27]. This further explains the characteristics of transmission peaks in Fig. 7. For the stacking arrangements ABA(B) and ABC(B), the transmission peak in the high frequency region is high and wide [black arrow in Fig. 7] because of the C-B matched interfaces, corresponding to stronger phonon coupling. For the configuration ABA(N), the transmission peak in the low frequency region is much stronger than the peak in the high frequency region [blue arrow in Fig. 7] resulting from the C-N matched interfaces.

Ⅳ. CONCLUSIONS

In summary, we have developed an atomistic framework based on DFT and atomistic Green's function to investigate the impact of different lattice stacking configurations on the thermal transport across the h-BN/graphene/h-BN interfaces. The h-BN substrates soften the TO and LO modes of graphene because of the overlap of orbitals and introduces an asymmetry between carbon atoms in graphene's unit cell leading to gap of different magnitude between the TA and ZA modes of graphene at K point in different stacking configurations. We find that the in-plane acoustic modes have the dominant contributions to the TBC for the C-B matched interfaces because of the low interfacial gap, but their contribution reduces as the interfacial separation distance increases. The frequency and wave vector dependent transmission reveal very low

transmission between 2-3 THz for ABA(N) configurations with C-N matched interface leading to sharp drop in TBC compared to other structures which has C-B matched interfaces. The TBC can be enhanced by more than 50% by changing the lattice stacking arrangements from C-N matched to C-B matched interface. Our results for TBC (32.5~50.0 MW/(m^2·K)) is closer to the experimental measurement compared to the previous studies. The findings in this study will provide insights to better understand the experimental measurements on TBC and the mechanism of phonon transport at h-BN/graphene/h-BN interfaces.

ACKNOWLEDGMENTS

This work was partially supported by UT Battelle LLC/Oak Ridge National Lab Grant under contract DE-AC05-00OR22725 and National Science Foundation Grant CBET-1236416. Part of this research was conducted at the Center for Nanophase Materials Sciences, which is a DOE Office of Science User Facility and supported by the ORNL Laboratory Directed Research and Development funding. This research used resources of the National Energy Research Scientific Computing Center, a DOE Office of Science User Facility supported by the Office of Science of the U.S. Department of Energy under Contract No. DE-AC02-05CH11231.

REFERENCES

1. K. Bourzac, *Nature*, 2012, **483**, S34-S36.
2. A. A. Balandin, *Nat Mater*, 2011, **10**, 569-581.
3. F. Schwierz, *Nat Nano*, 2010, **5**, 487-496.
4. X. Gu and R. Yang, *Journal of Applied Physics*, 2015, **117**, 025102.
5. C. R. Dean, A. F. Young, MericI, LeeC, WangL, SorgenfreiS, WatanabeK, TaniguchiT, KimP, K. L. Shepard and HoneJ, *Nat Nano*, 2010, **5**, 722-726.
6. A. K. Geim and K. S. Novoselov, *Nat Mater*, 2007, **6**, 183-191.
7. T. P. Kaloni, Y. C. Cheng and U. Schwingenschlogl, *J Mater Chem*, 2012, **22**, 919-922.

8. M. Freitag, M. Steiner, Y. Martin, V. Perebeinos, Z. Chen, J. C. Tsang and P. Avouris, *Nano Lett*, 2009, **9**, 1883-1888.
9. Y. K. Koh, M.-H. Bae, D. G. Cahill and E. Pop, *Nano Lett*, 2010, **10**, 4363-4368.
10. S. Xiong, K. Yang, Y. A. Kosevich, Y. Chalopin, R. D'Agosta, P. Cortona and S. Volz, *Physical Review Letters*, 2014, **112**, 114301.
11. M. Prunnila and J. Meltaus, *Physical Review Letters*, 2010, **105**, 125501.
12. V. Chiloyan, J. Garg, K. Esfarjani and G. Chen, *Nat Commun*, 2015, **6**.
13. C.-C. Chen, Z. Li, L. Shi and S. B. Cronin, *Applied Physics Letters*, 2014, **104**, -.
14. R. Mao, B. D. Kong, K. W. Kim, T. Jayasekera, A. Calzolari and M. Buongiorno Nardelli, *Applied Physics Letters*, 2012, **101**, 113111.
15. P. M. Norris, J. L. Smoyer, J. C. Duda and P. E. Hopkins, *Journal of Heat Transfer*, 2011, **134**, 020910-020910.
16. J. J. Gengler, S. V. Shenogin, J. E. Bultman, A. K. Roy, A. A. Voevodin and C. Muratore, *Journal of Applied Physics*, 2012, **112**, 094904.
17. L. Chen, Z. Huang and S. Kumar, *RSC Advances*, 2014, **4**, 35852-35861.
18. M. Shen, P. K. Schelling and P. Keblinski, *Physical Review B*, 2013, **88**, 045444.
19. J. M. Xue, J. Sanchez-Yamagishi, D. Bulmash, P. Jacquod, A. Deshpande, K. Watanabe, T. Taniguchi, P. Jarillo-Herrero and B. J. Leroy, *Nature Materials*, 2011, **10**, 282-285.
20. B. Sachs, T. O. Wehling, M. I. Katsnelson and A. I. Lichtenstein, *Physical Review B*, 2011, **84**, 195414.
21. G. Giovannetti, P. A. Khomyakov, G. Brocks, P. J. Kelly and J. van den Brink, *Physical Review B*, 2007, **76**.
22. X. L. Zhong, R. G. Amorim, R. H. Scheicher, R. Pandey and S. P. Karna, *Nanoscale*, 2012, **4**, 5490-5498.
23. J. Slawinska, I. Zasada, P. Kosinski and Z. Klusek, *Physical Review B*, 2010, **82**.
24. Y. J. Li, Q. Q. Sun, L. Chen, P. Zhou, P. F. Wang, S. J. Ding and D. W. Zhang, *Aip Adv*, 2012, **2**.
25. R. Quhe, J. X. Zheng, G. F. Luo, Q. H. Liu, R. Qin, J. Zhou, D. P. Yu, S. Nagase, W. N. Mei, Z. X. Gao and J. Lu, *Npg Asia Mater*, 2012, **4**.
26. M. Pashangpour, Z. Bagheri and V. Ghaffari, *Eur Phys J B*, 2013, **86**.
27. G. J. Slotman, G. A. de Wijs, A. Fasolino and M. I. Katsnelson, *Ann Phys-Berlin*, 2014, **526**, 381-386.
28. G. Kresse and J. Furthmuller, *Comp Mater Sci*, 1996, **6**, 15-50.
29. W. Zhang, T. S. Fisher and N. Mingo, *Numer Heat Tr B-Fund*, 2007, **51**, 333-349.
30. W. Zhang, T. S. Fisher and N. Mingo, *J Heat Trans-T Asme*, 2007, **129**, 483-491.
31. Z. Tian, K. Esfarjani and G. Chen, *Physical Review B*, 2012, **86**, 235304.
32. D. A. Stewart, I. Savic and N. Mingo, *Nano Lett*, 2008, **9**, 81-84.
33. E. Munoz, J. Lu and B. I. Yakobson, *Nano Lett*, 2010, **10**, 1652-1656.
34. G. Kern, G. Kresse and J. Hafner, *Physical Review B*, 1999, **59**, 8551.
35. X. Wu and T. Luo, *Journal of Applied Physics*, 2014, **115**, 014901.
36. S. Sadasivam, Y. Che, Z. Huang, L. Chen, S. Kumar and T. S. Fisher, *Ann. Rev. Heat Transfer*, 2014, **17**, 89-145.
37. S. Baroni, S. De Gironcoli, A. Dal Corso and P. Giannozzi, *Reviews of Modern Physics*, 2001, **73**, 515.
38. Y. Chalopin, S. Volz and N. Mingo, *Journal of Applied Physics*, 2009, **105**, 084301.
39. X. Gu, X. Li and R. Yang, *Physical Review B*, 2015, **91**, 205313.
40. N. Mingo, *Physical Review B*, 2006, **74**, 125402.
41. X. Zhong, Y. K. Yap, R. Pandey and S. P. Karna, *Physical Review B*, 2011, **83**, 193403.
42. G. Kresse and D. Joubert, *Physical Review B*, 1999, **59**, 1758-1775.

43. J. P. Perdew, *Physical Review B*, 1986, **33**, 8822-8824.
44. A. Marini, P. García-González and A. Rubio, *Physical Review Letters*, 2006, **96**, 136404.
45. J.-C. Charlier, X. Gonze and J.-P. Michenaud, *EPL (Europhysics Letters)*, 1994, **28**, 403.
46. W. J. Yu, W. M. Lau, S. P. Chan, Z. F. Liu and Q. Q. Zheng, *Physical Review B*, 2003, **67**, 014108.
47. H. Rydberg, M. Dion, N. Jacobson, E. Schröder, P. Hyldgaard, S. I. Simak, D. C. Langreth and B. I. Lundqvist, *Physical Review Letters*, 2003, **91**, 126402.
48. L. Chen, Z. Huang and S. Kumar, *Applied Physics Letters*, 2013, **103**, 123110.
49. R. W. Lynch and H. G. Drickamer, *The Journal of Chemical Physics*, 1966, **44**, 181-184.
50. N. Mingo, D. A. Stewart, D. A. Broido and D. Srivastava, 2008.
51. A. Dhar and D. Roy, *J Stat Phys*, 2006, **125**, 801-820.
52. H. J. Monkhorst and J. D. Pack, *Physical Review B*, 1976, **13**, 5188-5192.
53. N. Ooi, V. Rajan, J. Gottlieb, Y. Catherine and J. Adams, *Modelling and Simulation in Materials Science and Engineering*, 2006, **14**, 515.
54. C. Oshima and A. Nagashima, *Journal of Physics: Condensed Matter*, 1997, **9**, 1.
55. A. M. Shikin, V. K. Adamchuk and K. H. Rieder, *Phys. Solid State*, 2009, **51**, 2390-2400.
56. A. M. Shikin, G. V. Prudnikova, V. K. Adamchuk, F. Moresco and K. H. Rieder, *Physical Review B*, 2000, **62**, 13202-13208.
57. A. Allard and L. Wirtz, *Nano Lett*, 2010, **10**, 4335-4340.
58. A. Ramasubramaniam, D. Naveh and E. Towe, *Nano Lett*, 2011, **11**, 1070-1075.
59. P. Khomyakov, G. Giovannetti, P. Rusu, G. Brocks, J. Van den Brink and P. Kelly, *Physical Review B*, 2009, **79**, 195425.
60. T. Beechem, L. Yates and S. Graham, *Review of Scientific Instruments*, 2015, **86**, 041101.
61. X. Li and R. Yang, *Physical Review B*, 2012, **86**, 054305.

TABLE

Table 1. Properties of h-BN/graphene/h-BN sandwiched structure with different lattice stacking arrangements.

Structure	Separation distance (Å)	TBC at room temperature ($MW/m^2 \cdot K$)	ZO/ZA gap at K point (THz)
ABC(B)	3.23	50.0	0
ABA(B)	3.23	46.6	0.24
ABA(N)	3.45	32.5	0.15
AAA	3.51	43.1	0.25
ABC(N,B)	3.45, 3.23	40.8	0.22

FIGURE CAPTIONS

FIG. 1. Side views of the five lattice stacking configurations of SLG sandwiched between h-BN layers in x-y plane and x-z plane. d_1 and d_2 presents the interfacial separation distances. The brown, green, and gray spheres represent carbon, boron, and nitrogen atoms, respectively.

FIG. 2. Schematic diagram of h-BN/SLG/h-BN sandwiched system for the AGF calculations. The system is divided into a 'device' region (D), left contact (LC) and right contact (RC) and two semi-infinite h-BN bulks, left contact bulk (LCB) and right contact bulk (RCB) which do not interact with the 'device' region. The 'device' region only includes the SLG layer.

FIG. 3. Phonon dispersions of (a) isolated SLG, stretched isolated SLG and SLG (stretched) in the ABA(B) sandwiched structure; (b-e) isolated SLG and SLG (stretched) in ABA(N), AAA, ABC(B), ABC(N,B) sandwiched structures, respectively. The splitting at K point between ZA and ZO modes are marked with red rectangles and also shown in inset as extended view.

FIG. 4. DOSs of isolated SLG, stretched isolated SLG, h-BN and SLG (stretched) sandwiched by h-BN with different stacking configurations.

FIG. 5. (a) Temperature dependent thermal boundary conductance at h-BN/SLG/h-BN interfaces for different lattice stacking configurations. (b) Frequency dependent thermal boundary conductance at h-BN/SLG/h-BN interfaces for different lattice stacking configurations.

FIG. 6. Plane-averaged electron density difference Δn (per unit cell) along out of plane direction showing the charge redistribution at the h-BN/graphene/h-BN interfaces. $-e$ is the charge of an electron. Here, Δn represents the difference in the plane-averaged electron density of the sandwiched structure from h-BN layers and free-standing graphene.

FIG. 7. Angular frequency dependent phonon transmission for different lattice stacking configurations. Inset shows phonon transmission for frequency in the range of 0-8 THz. Blue arrow shows peak in transmission for ABA(N) for modes where contribution of N atoms is

higher and black arrow shows peak in transmission for ABA(B) for modes where contribution of B atoms is higher.

FIG. 8. Frequency and wave vector dependent phonon transmission along $\Gamma - K$ direction for different stacking configurations. Black dashed lines in (a-e) show phonon dispersion (<5 THz) of SLG in the sandwiched structures along $\Gamma - K$ direction. Black dashed lines in (f-j) shown phonon dispersion (<5 THz) of entire sandwiched structure along $\Gamma - K$ direction.

FIGURES

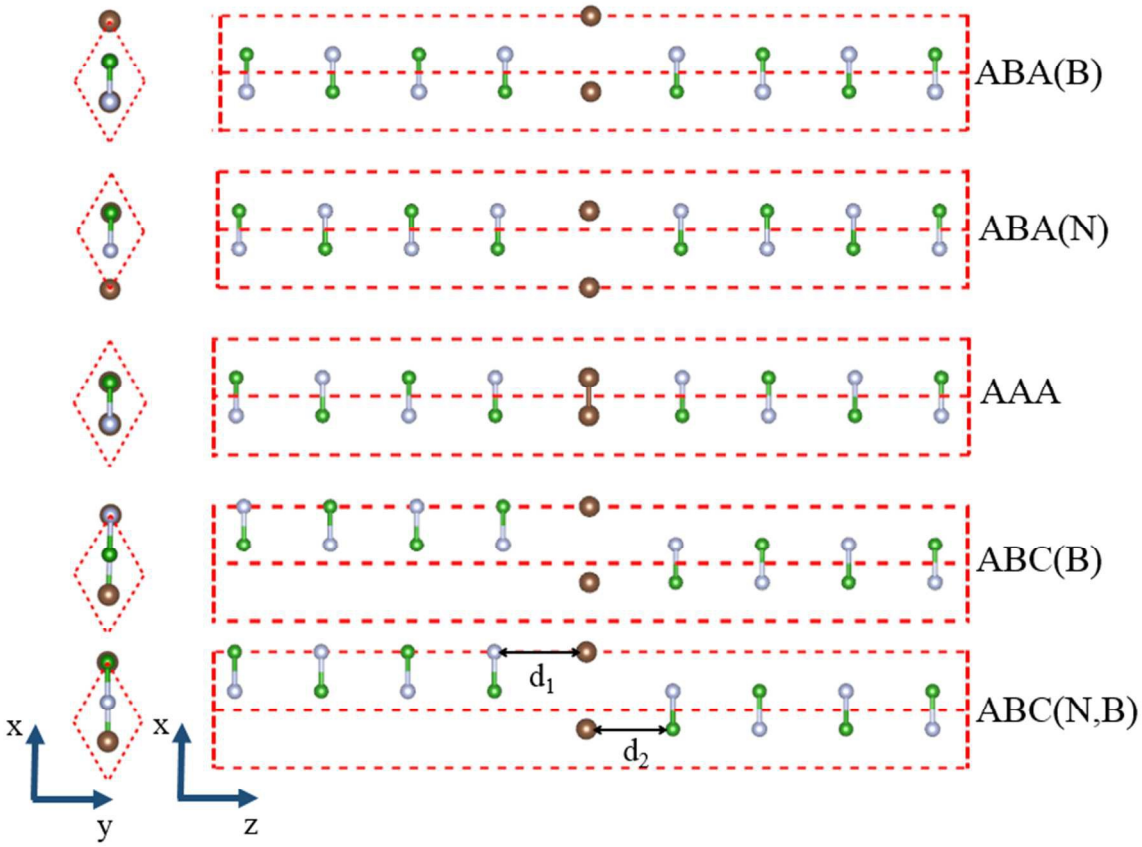

FIG. 1. Side views of the five lattice stacking configurations of SLG sandwiched between h-BN layers in x-y plane and x-z plane. d_1 and d_2 presents the interfacial separation distances. The brown, green, and gray spheres represent carbon, boron, and nitrogen atoms, respectively.

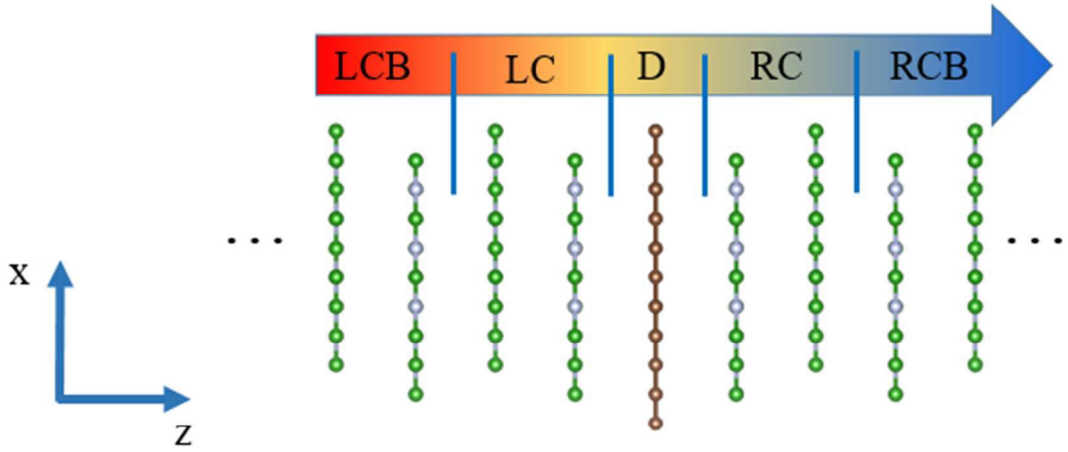

FIG. 2. Schematic diagram of h-BN/SLG/h-BN sandwiched system for the AGF calculations. The system is divided into a 'device' region (D), left contact (LC) and right contact (RC) and two semi-infinite h-BN bulks, left contact bulk (LCB) and right contact bulk (RCB) which do not interact with the 'device' region. The 'device' region only includes the SLG layer.

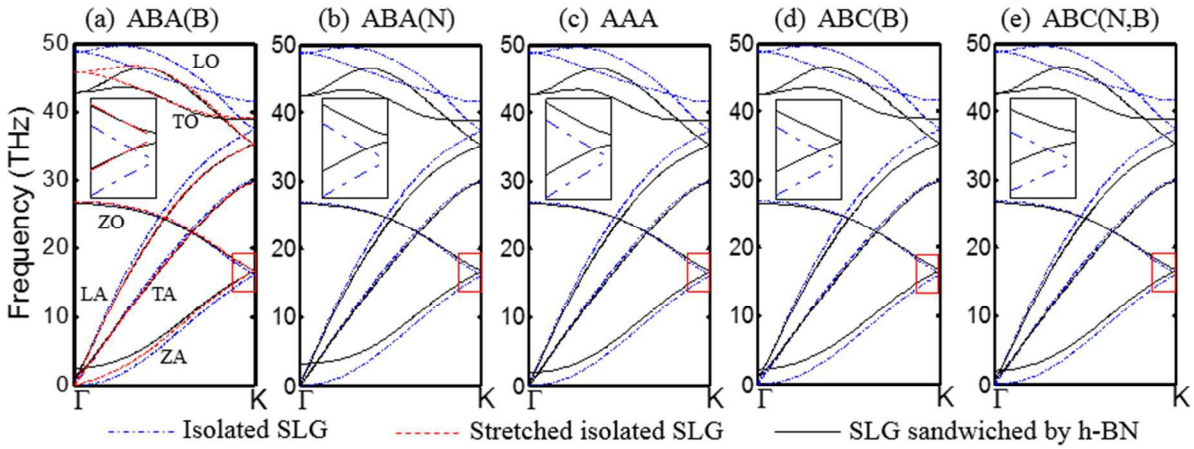

FIG. 3. Phonon dispersions of (a) isolated SLG, stretched isolated SLG and SLG (stretched) in the ABA(B) sandwiched structure; (b-e) isolated SLG and SLG (stretched) in ABA(N), AAA, ABC(B), ABC(N,B) sandwiched structures, respectively. The splitting at K point between ZA and ZO modes are marked with red rectangles and also shown in inset as extended view.

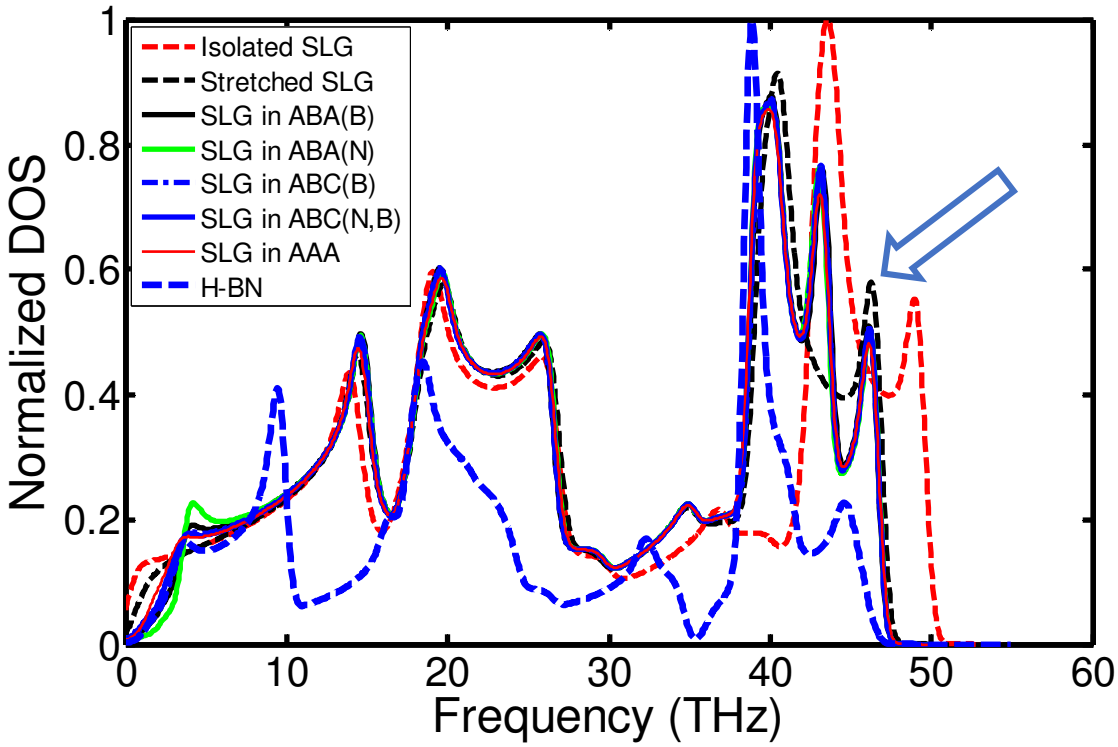

FIG. 4. DOSs of isolated SLG, stretched isolated SLG, h-BN and SLG (stretched) sandwiched by h-BN with different stacking configurations.

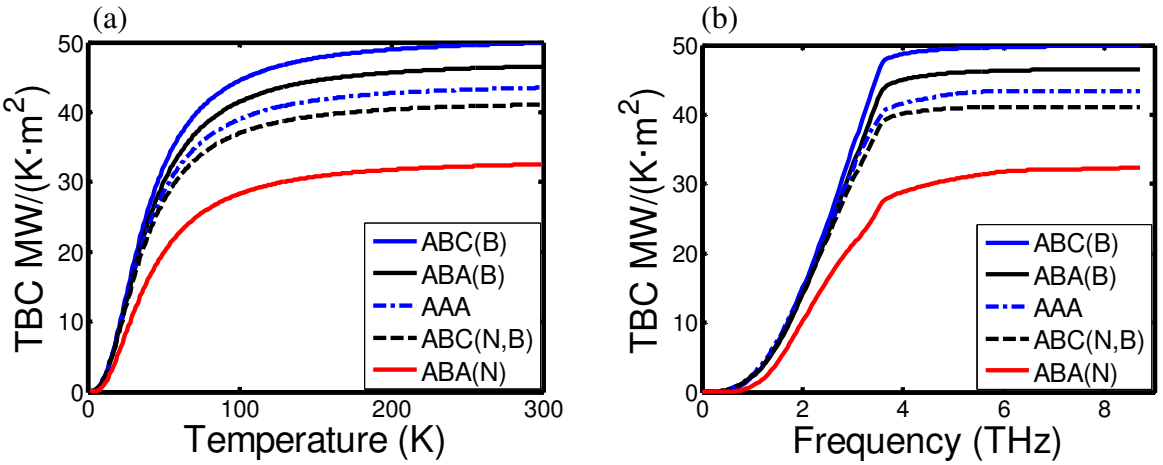

FIG. 5. (a) Temperature dependent thermal boundary conductance at h-BN/SLG/h-BN interfaces for different lattice stacking configurations. (b) Frequency dependent thermal boundary conductance at h-BN/SLG/h-BN interfaces for different lattice stacking configurations at room temperature.

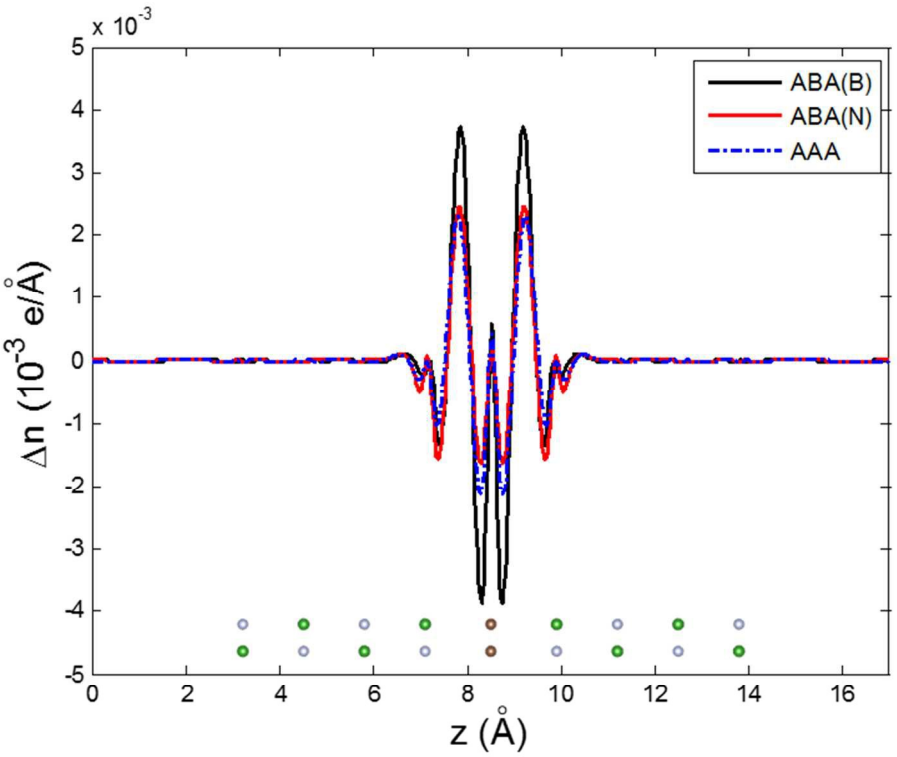

FIG. 6. Plane-averaged electron density difference Δn (per unit cell) along out of plane direction showing the charge redistribution at the h-BN/graphene/h-BN interfaces. $-e$ is the charge of an electron. Here, Δn represents the difference in the plane-averaged electron density of the sandwiched structure from h-BN layers and free-standing graphene.

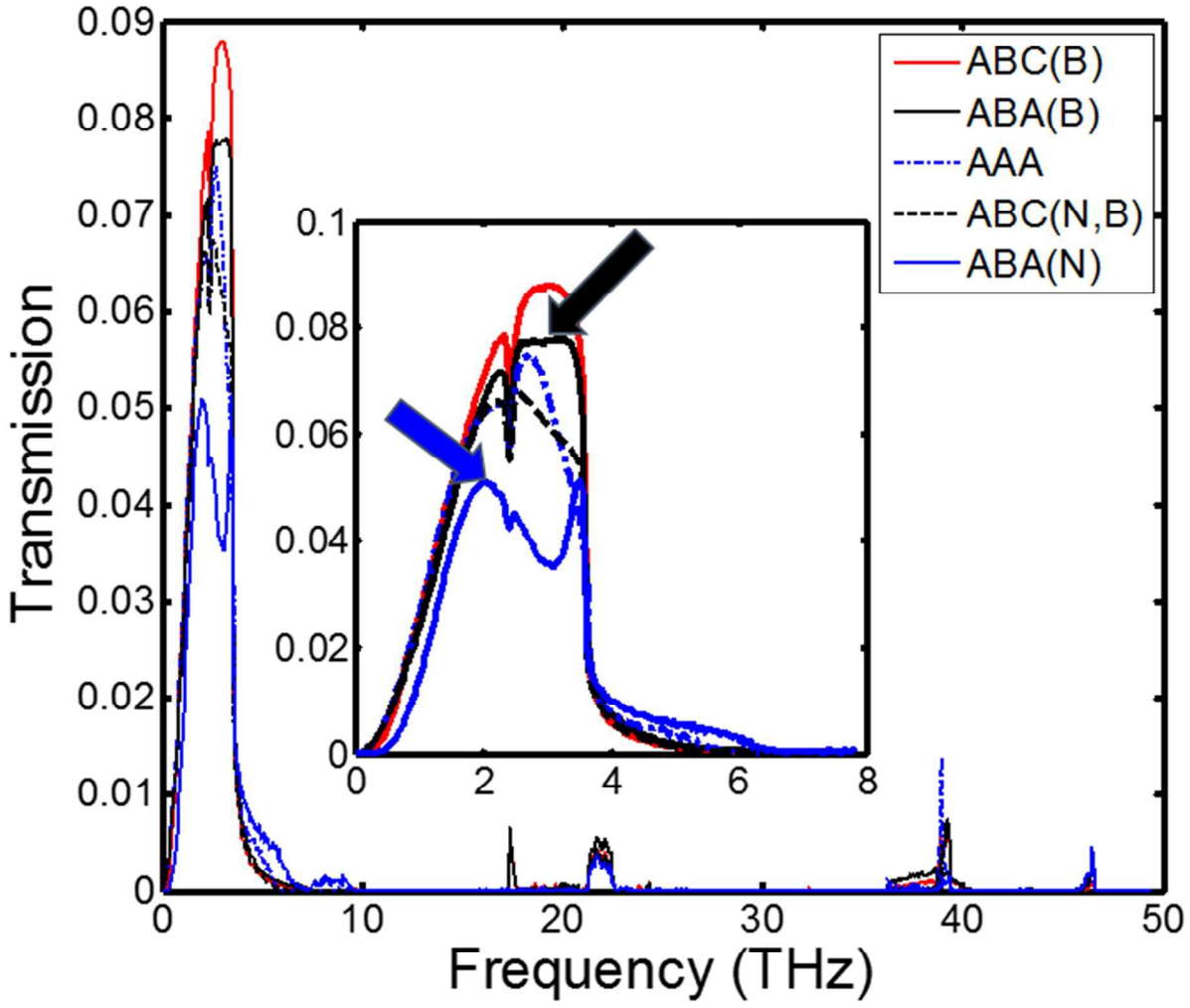

FIG. 7. Angular frequency dependent phonon transmission for different lattice stacking configurations. Inset shows phonon transmission for frequency in the range of 0-8 THz. Blue arrow shows peak in transmission for ABA(N) for modes where contribution of N atoms is higher and black arrow shows peak in transmission for ABA(B) for modes where contribution of B atoms is higher.

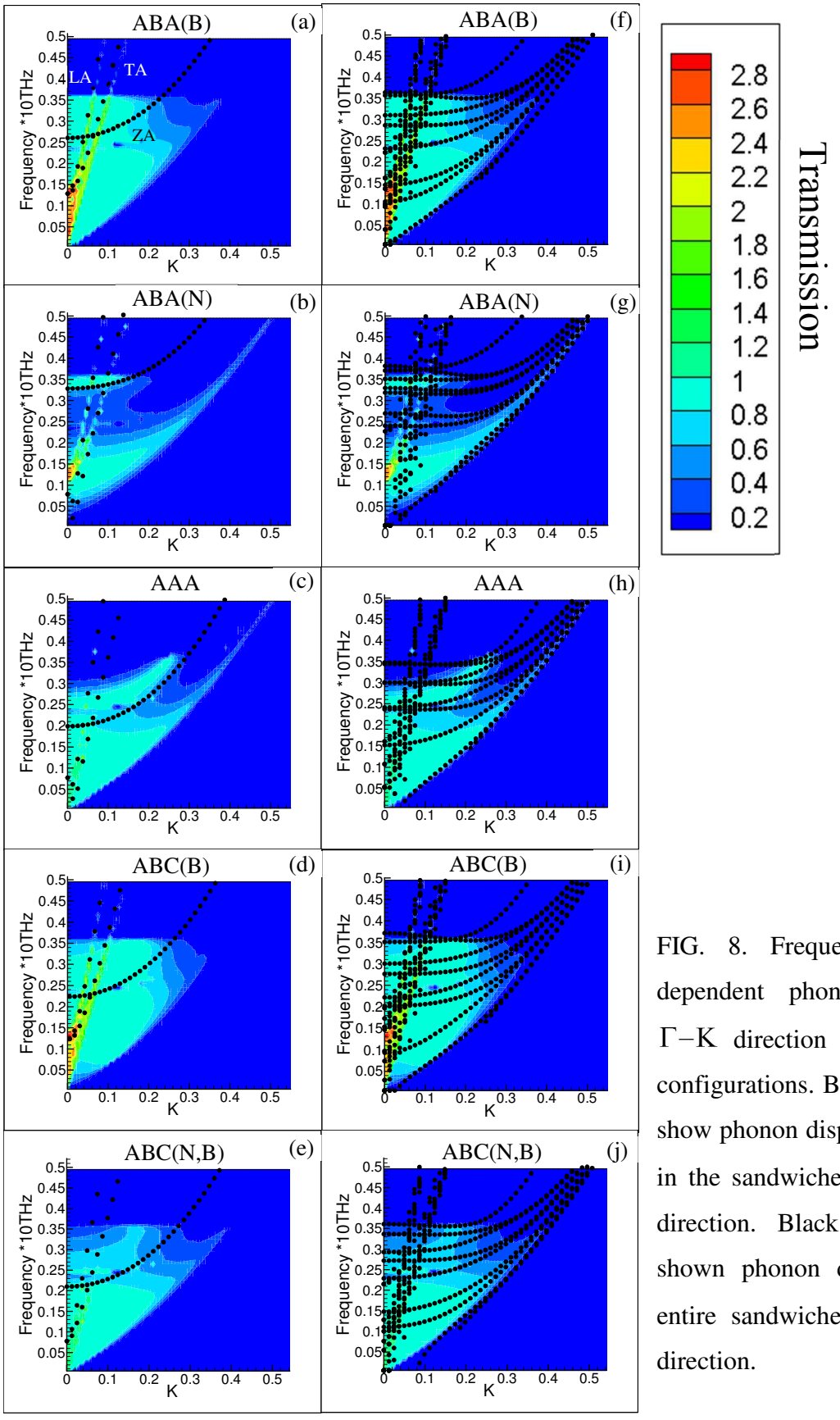

FIG. 8. Frequency and wave vector dependent phonon transmission along $\Gamma-K$ direction for different stacking configurations. Black dashed lines in (a-e) show phonon dispersion (<5 THz) of SLG in the sandwiched structures along $\Gamma-K$ direction. Black dashed lines in (f-j) shown phonon dispersion (<5 THz) of entire sandwiched structure along $\Gamma-K$ direction.